TECHNICAL ARTICLE

Bimodal microstructural characterization of Si powder using X-ray diffraction: the role of peak shape

Ashok Bhakar [1,2,a)] Himanshu Srivastava,[1] Pragya Tiwari,[1] and S. K. Rai[1,2]

[1]*Accelerator Physics and Synchrotrons Utilization Division, Raja Ramanna Centre for Advanced Technology, Indore 452013, India*

[2]*Homi Bhabha National Institute, Training School Complex, Anushakti Nagar, Mumbai 400094, India*

X-ray diffraction (XRD) characterization of Si powder was carried out using synchrotron and laboratory sources. Microstructural (size-strain) analyses of XRD patterns were carried out using the Rietveld refinement method. Experimentally observed super-Lorentzian shapes of the XRD peaks of Si powder were examined using multimodal profile fitting and bimodal model was found to be adequate. The two components obtained using a bimodal approach are referred as narrow and broad profiles based on their estimated relative peak widths. Peak shapes of crystallite size-dependent parts of narrow and broad profiles were found to be almost Gaussian and Lorentzian in nature, respectively. The simultaneous presence of such peak shapes corresponding to a bimodal microstructure is uncommon in literature. Therefore, in order to explore the role of different natures of XRD peak shapes (size dependent) of the bimodal profiles of Si, detailed microstructural analysis was carried out using the complementary method of whole powder pattern modeling (WPPM) and found to be related to the variance of crystallites' size distribution. Additionally, the effect of instrument resolution (laboratory and synchrotron sources) on the microstructural parameters was also studied. Scanning and transmission electron microscopy were used to characterize the morphology of Si powder and correlate with the microstructural findings of XRD methods.

I. INTRODUCTION

Silicon (Si) has a wide range of applications in the field of semiconductor industry. Besides its traditional use in electronic devices, Si (in the form of porous and nanoparticles) has applications in several areas of optical materials (luminescent and light-emitting devices, photovoltaic industry) (Iyer and Xie, 1993; Miller, 1995; Pavesi et al., 2000; Cheng et al., 2011; Dhara and Giri, 2011; Desta et al., 2016), imaging and sensing for advanced biomedical therapies (Erogbogbo et al., 2011; Peng et al., 2014), solar cells and lithium-ion batteries (Su et al., 2014; Dutta et al., 2015; Zhang et al., 2021), hydrogen production (Erogbogbo et al., 2013; Bhisikar et al., 2022), agriculture (Rastogi et al., 2019; Bhat et al., 2021), mechanical alloys (Figueiredo and Margarido, 1997), etc. The abundance of Si and low cost of its polycrystalline form compared to single crystal form makes it a suitable candidate for large-scale industrial use and production. For a number of applications, small grain sizes (in nm) are desirable. Moreover, tailoring of particle or crystallite sizes affects the physical and chemical properties of the materials and plays a vital role in optimizing the performance of these devices (Garnier et al., 2019).

The properties of nanomaterials depend on the size, shape, and distribution of crystallites. Powder diffraction is a commonly used non-destructive and non-contact method to identify and quantify crystalline phases and is used for characterizing structural and microstructural (size-strain) properties of the crystalline materials (Snyder et al., 1999; Kaduk et al., 2021). The diffraction pattern is a convolution of microstructural parameters related to the crystallite domain sizes at nanoscale level and crystalline defects. Detailed microstructural information can be obtained from the width (also termed as breadth) and the shape of diffraction peaks and their behavior with scattering angle. In this regard, the study of the evolution of diffraction peak profile (shape and width) of the whole diffraction pattern is crucial for extracting size-strain contributions (Klug and Alexander, 1974; Matyi et al., 1987; Warren, 1990; Snyder et al., 1999; Cullity and Stock, 2001; Mittemeijer and Scardi, 2004; Weidenthaler, 2011; Gubicza, 2014; Thakral et al., 2016; Mourdikoudis et al., 2018). Several methods are available to deconvolve the contribution of the size-strain effects (Warren, 1990; Snyder et al., 1999; Cullity and Stock, 2001). These are broadly classified into two categories: (i) *peak broadening analysis* (PBA) and (ii) *peak profile analysis* (PPA) (Bhakar et al., 2023).

PBA utilizes only the width (either full width at half maximum (FWHM) or integral breadth (IB)) part of diffraction

---

peaks and commonly known as "breadth based methods" such as Scherrer formula (Scherrer, 1918), *Williamson–Hall* (WH) plot (Williamson and Hall, 1953), and modified-WH plot (Ungár and Borbély, 1996). These methods include analysis of single-peak or multiple-peaks or *whole powder pattern fitting* (WPPF). WPPF is implemented in various Rietveld refinement programs and also pursued in this study (Rietveld, 1967, 1969). In these methods, the role of diffraction peak shapes is unclear. Sometimes, the Gaussian peak shapes are assumed due to the size-effect (Scherrer, 1918; Williamson and Hall, 1953; Borchert et al., 2005; Bhakar et al., 2017). Contrary to this, several authors have considered Lorentzian peak shapes to attribute the nature of the size-broadening contribution in PBA (Williamson and Hall, 1953; Nandi and Sen Gupta, 1978; de Keijser et al., 1982, 1983; Delhez et al., 1982, 1988; Langford et al., 1988; Warren, 1990; Ungár and Borbély, 1996; Uvarov and Popov, 2015). Similarly, the manifestation of microstrain broadening is considered either Gaussian or Lorentzian as documented in the literature. Further use of the Voigt approximation is also common in WPPF (Langford, 1978; Balzar, 1992, 1999; Balzar and Ledbetter, 1993, 1994; Snyder et al., 1999; Balzar et al., 2004; Sánchez-Bajo et al., 2006; Ectors and Neubauer, 2015; Ectors et al., 2017; Scardi, 2020). Although, the Voigt approximation allows different types of peak shapes due to size-strain effect, it does not tell how these peak shapes are related to size-strain parameters. Probably due to this reason, the role of diffraction peak shapes is largely ignored in the PBA (Bhakar et al., 2023).

In contrast to breadth-based methods, alternative ways of PPA based on the Fourier analysis of diffraction peaks are also available like *Warren–Averbach* (WA) method (Warren and Averbach, 1950; Warren, 1990), modified-WA method (Ungár and Borbély, 1996), and *whole powder pattern modeling* (WPPM) (Gubicza et al., 2000; Ungár et al., 2001; Scardi and Leoni, 2002; Matěj et al., 2014; Scardi, 2020). In this approach, both the width and shape of the diffraction peaks are exploited to provide information on the domain sizes and their distribution. Both WPPF and WPPM methods are relatively newer compared to their counterparts and compared in literature (Scardi et al., 2001, 2004, 2006; Scardi, 2002; Ribárik et al., 2020). In WPPF, empirical profile functions (e.g. pseudo-Voigt) are chosen (based on observations) for better fitting of the whole diffraction pattern without bothering about their origin and relation with the microstructure of the samples. Whereas in the case of WPPM, peak profiles are described using the physical models directly related to the microstructure of the materials. Differences between the microstructural parameters obtained using WPPF and WPPM approaches are frequently highlighted in the literature (Scardi et al., 2001, 2004, 2006; Scardi, 2002; Ribárik et al., 2020). Despite these differences, there is a common similarity that both approaches give almost equivalent quality of fitting to diffraction patterns in most of the cases. Recently Bhakar et al. have explored this similarity and derived a relationship between the size parameters obtained using the WPPF and WPPM through diffraction peak shapes (Bhakar et al., 2023). It has facilitated the comparison of both the methods (which are otherwise believed to be non-comparable) and used to study unimodal microstructures only. For its generalized use, the studies over complex/multimodal microstructures are needed. Therefore, the motivation of this work is to investigate the appropriateness of this peak shape strategy on Si powder sample which is characterized using a bimodal microstructure.

In this work, experimentally observed super-Lorentzian peak shapes of the XRD pattern of the Si powder were analyzed using unimodal and bimodal microstructural profile fitting. Although a broad lognormal size distribution (unimodal) alone (Langford et al., 2000; Popa and Balzar, 2002, 2008; Ida et al., 2003) or the existence of bimodal (Young and Sakthivel, 1988; Deb et al., 2007; Ram et al., 2009; Matěj et al., 2014; Uvarov and Popov, 2015; Wang et al., 2015; Bhakar et al., 2021; Baral et al., 2022) or multimodal (in general) microstructural contribution can lead to super-Lorentzian peak shapes. But in the present work, the usage of unimodal analysis gives a systematic mismatch between the observed and calculated diffraction patterns. This mismatch increases with increasing scattering angle (better visualization was possible from the analysis of synchrotron XRD data compared to laboratory XRD data). Therefore, bimodal analysis was carried out and adequate profile fitting was observed. Thus, analyses are restricted to uni- and bimodal models. The two components of microstructure obtained using a bimodal WPPF analysis are referred to as narrow and broad profiles based on their estimated relative peak widths derived from the Rietveld refinement. The microstructural contribution to the diffraction peak shapes corresponding to (only) size-broadening part of narrow and broad profiles were found to be almost Gaussian and Lorentzian in nature, respectively. Simultaneous presence of such bimodal peak profiles (having different peak shapes) in a powder sample is rare and detailed microstructural characterization of such behavior is rather scanty in the literature. Also, the physical significance of observed diffraction peak shapes (in WPPF approaches) is unclear. In order to emphasize the significance of XRD peak shapes, the WPPM analysis was carried out and compared with WPPF. The nature of diffraction peak shapes is found to be related to the distribution of crystallites/domain sizes (Bhakar et al., 2023). Additionally, the effect of the instrument resolution on the microstructural parameters obtained from the XRD analysis of two different instruments (laboratory and synchrotron source) is discussed. Dynamic light scattering (DLS) and, scanning and transmission electron microscopy were used to characterize Si powder and correlate with the results obtained from PPA.

II. EXPERIMENTAL DETAILS

A. Sample characterization methods

Room temperature synchrotron XRD measurements of *National Institute of Standards and Technology* (NIST, 2010) *Standard Reference Material* (SRM) Si 640d and as-received Si powder (purity 99.999%; Lot #J27U037; ACI Alloys Inc., USA) were carried out at Engineering Applications Beamline (BL-02) of *Indus-2 synchrotron source, India* (Gupta et al., 2021). Hereafter, these two powders are abbreviated as SRM 640d powder and Si powder, respectively. Measurements were carried out in reflection geometry and monochromatic high-resolution focus beam θ–2θ mode of beamline using Huber diffractometer and Dectris detector (MYTHEN2 X 1K) at wavelength $\lambda \sim$ 1.0353(1) Å. In this mode of beamline cylindrical pre-mirror (M1), double crystal monochromator (DCM with Si 111

single crystal pair) and toroidal post-mirror (M2) were used. The distances of the M1, DCM, M2, and MYTHEN position-sensitive detector (PSD) are ~17.2, 21.2, 24, and 36 m, respectively, from the synchrotron beam source point at the bending magnet. Two Si powders were filled in a glass sample holder of diameter 15 mm and thickness ~0.15 mm and rotated at ~45 rpm during measurements (Bhakar et al., 2021). The beam size was defined using slits of ~2.5 mm (H) × 0.25 mm (V) opening in the path of the incident beam placed at a distance of ~800 mm from the goniometer center. Position-sensitive detector was installed at a distance of ~1067 mm from the goniometer center for recording diffraction patterns. It can cover a total 2θ range of ~3.43164° per frame (out of which effective span size was chosen as 3.3244° by removing datum of 20 pixels on both end sides of the PSD). PSD was moved in steps of 1.0107° (total 103 steps to complete the measurement). In this way, the XRD data at each 2θ point was measured thrice and averaged to reduce the noise level. XRD data acquisition time at each step was 45 and 70 s for SRM 640d and as-received Si powders, respectively. The details of DLS and Laboratory XRD measurements are provided in the Supplementary information file associated with this manuscript. Morphology of the Si powder was characterized using *scanning electron microscope* (SEM), Philips, XL30 CP and *transmission electron microscope* (TEM), Philips, CM200. The sample for SEM was prepared by dispersing Si powder in isopropyl alcohol by ultrasonication and drop casting the resultant suspension on a polished germanium (Ge) wafer. The sample for TEM was prepared by dropcasting the Si powder suspension of appropriate concentration on a formvar/carbon-coated Cu grid.

B. XRD data analysis using WPPF and WPPM methods

In WPPF approach, *FullProf* software (Rodríguez-Carvajal, 1993) was used for the Rietveld refinement (Rietveld, 1967, 1969) and Le Bail fitting (Le Bail et al., 1988) of XRD data of Si powder using *pseudo-Voigt* (pV) and *Thompson–Cox–Hastings* (TCH) peak profile functions (Thompson et al., 1987; Finger et al., 1994). The atomic co-ordinates of Si were kept fixed at *8a (1/8, 1/8, 1/8)* Wyckoff positions (space group*: Fd3̄m*) and isotropic atomic displacement parameters (ADPs/B_{iso}) were refined. Other parameters, i.e. scale factor, instrument 2θ corrections, low angle asymmetry of the peak profile, unit cell parameters, peak profile half-width/microstructural parameters, preferred orientation, and background (Chebyshev polynomial) were refined. The details of PPA using the pV function are given in the supplementary file and analysis using TCH profile function is described here in brief (Rodríguez-Carvajal and Roisnel, 2004). For isotropic peak profiles (applicable in this study), the angular dependence of Gaussian (H_G) and Lorentzian (H_L) contribution to total FWHM (H) using the TCH profile function are given by the following expressions:

$$H_G^2 = U\tan^2\theta + V\tan\theta + W + \frac{I_G}{\cos^2\theta} \qquad (1)$$

$$H_L = X\tan\theta + \frac{Y}{\cos\theta} \qquad (2)$$

Here U, V, W, I_G, (units in degrees square) and X, Y (units in degrees) are refinable parameters. To account for the
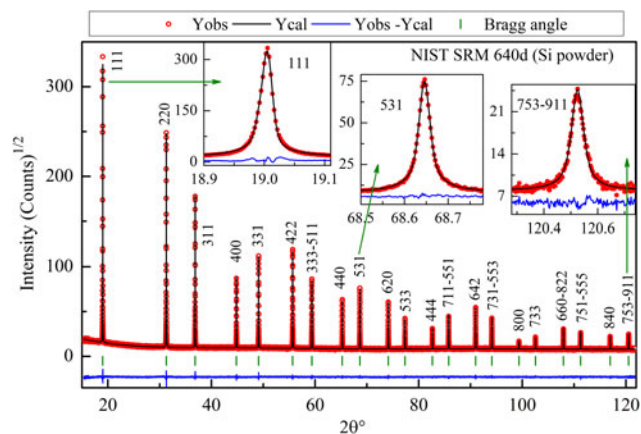

Figure 1. Le Bail fitting of synchrotron XRD data of NIST SRM 640d using TCH function (refined $\lambda \sim 1.0353(1)$ Å). Insets show the fitting quality of three Bragg peaks across the full 2θ range. Red circles represent the synchrotron powder XRD data, and black and blue lines represent the fitted curve and difference curve, respectively. The green vertical ticks correspond to the Bragg positions with corresponding *hkl* indices. The Rietveld *R* factors (not corrected for background) are R_p 5.3%, R_{wp} 6.9%, R_{exp} 8.2%, and χ^2 0.71.

instrumental contribution of synchrotron beamline BL-02, an instrument resolution function (IRF) was prepared by analyzing XRD data of NIST Si powder (SRM 640d) using the TCH profile function (Bhakar et al., 2017) and the resulting profile fitting is shown in Figure 1. The usefulness of choosing the TCH profile function and including IRF file is that TCH parameters I_G & Y and U & X are directly related to the Gaussian and Lorentzian contributions of the size and strain broadening, respectively. Another feature of TCH formulation is that its implementation restricts η values between 0 and 1. Attempts were made for anisotropic (unimodal and bimodal) microstructural analysis of Si powder but the improvement was insignificant; therefore, only isotropic WPPF analyses were carried out. Further details of the procedure adopted are the same as reported in the literature (Rodríguez-Carvajal and Roisnel, 2004; Bhakar et al., 2017).

The WPPM analysis was performed using *PM2K* software version 2.12 (Scardi and Leoni, 2002; Leoni et al., 2006; Scardi, 2020). In this approach, Fourier method is applied to simulate the observed diffraction peak profiles. The microstructural contributions of the sample were calculated from the convolution of physical models suitable for the crystallite sizes and crystal defects (vacancies, dislocations, stacking, twin faults, etc.) related effects. The intensity (reciprocal space) of the experimental profile is mathematically described by the following equation (Scardi et al., 2000):

$$I(d^*) = k(d^*)\int A(L)\exp(2\pi i L d_{hkl}^*)dL \qquad (3)$$

where $d^* = 2\sin\theta/\lambda$ is diffraction vector in reciprocal space and d_{hkl}^* is diffraction vector corresponding to Bragg (*hkl*) peaks. θ is the scattering angle, L is the Fourier variable in direct space, and $k(d^*)$ contains all geometrical and structural related parameters contributing to the intensity of the diffraction peak (like multiplicity, Lorentz-polarization, structure factor, etc.). The Fourier coefficient, $A(L)$ carries peak profile information and is a product of Fourier Transformation components associated with IRF, domain size distribution,

dislocations, faulting, etc. For modeling crystallite size distribution of Si powder lognormal distribution of spherical shape was used. A lognormal distribution for crystallite of spherical diameter D is defined as (Scardi et al., 2004):

$$g(D) = \frac{1}{D\sigma\sqrt{2\pi}} \exp\left[-\frac{1}{2}\left(\frac{\ln D - \mu}{\sigma}\right)^2\right] \quad (4)$$

where μ and σ^2 are lognormal mean and lognormal variance of size distribution. For this distribution, the various mean sizes were calculated using the following expression: $\exp(\mu + N\sigma^2/2)$. The values 1, 5, and 7 for constant N in this expression correspond to the arithmetic (D_M), surface (D_S), volume (D_V) weighted mean domain sizes, and standard deviation (s.d.) given by: $\sqrt{\{\exp(2\mu + \sigma^2) \times (\exp(\sigma^2) - 1)\}}$ (Langford et al., 2000; Popa and Balzar, 2002).

The peak broadening effect related to dislocations was modeled by using the Wilkens theory (Wilkens, 1970, 1987) and the expression for Fourier coefficients due to dislocations is:

$$A^D(L) = \exp\left[-\frac{1}{2}\pi|\boldsymbol{b}|^2\bar{C}_{hkl}\rho d_{hkl}^{*2}L^2 f^*\left(\frac{L}{R_e}\right)\right] \quad (5)$$

where ρ is the average dislocation density, R_e is effective outer cut-off radius, $\bar{C}_{hkl}$ is the average hkl-dependent contrast factor, and $f^*(L/R_e)$ is the Wilkens function (Wilkens, 1970). For estimating dislocation density, the $\{111\}\langle 11\,0\rangle$ slip system of fcc (face-centered cubic) crystal structure was considered, for which Burgers vector modulus is given as $b = a_0 \times \sqrt{2}/2$, here a_0 is the lattice constant. The hkl-dependent (anisotropic) average contrast factor of dislocations $\bar{C}$ in cubic crystals is given by (Ungár et al., 1999):

$$\bar{C} \equiv \bar{C}_{hkl} = A + BH^2 \quad (6)$$

Here $H^2 = (h^2k^2 + k^2l^2 + l^2h^2)/(h^2 + k^2 + l^2)^2$; h, k, l are indices of the diffraction peak. A and B are constants related to the nature of dislocations (screw and edge) and elastic constants of the crystal. Their average values were calculated using the ANIZC program (Borbély et al., 2003) using elastic constants $C_{11} = 166$ GPa, $C_{12} = 64$ GPa, and $C_{44} = 80$ GPa of Si. For edge and screw dislocations these values are 0.20874 (Ascrew), -0.360 (Bscrew), 0.2127 (Aedge), and -0.1586 (Bedge) and matching with literature (Dhara and Giri, 2011). Using these values, the relative fraction of edge dislocations (f_E) was refined. For pure edge and pure screw dislocation character, $f_E = 1$ and 0, respectively. Background was modeled using the Chebyshev polynomial.

III. RESULTS

A. Examination of XRD peak shapes using pV profile function

Synchrotron XRD pattern of Si powder corresponds to the fcc phase. Comparison of a few Bragg peaks (across the full 2θ range) of this diffraction pattern with SRM 640d Si powder is shown in Figure 2, which shows that the peak positions of both the samples are closely matched. However, the width (FWHM) and the tails of Bragg peaks of Si powder are significantly broader than the corresponding Bragg peaks of SRM
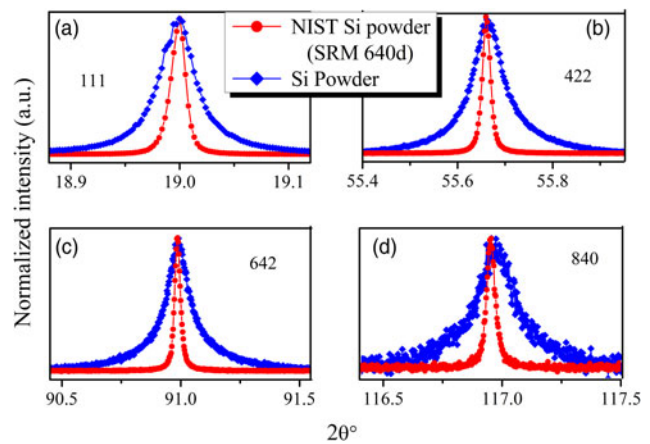

Figure 2. Comparison of peak profiles of synchrotron powder XRD data ($\lambda \sim 1.0353(1)$ Å) of SRM 640d Si powder (red circles) with Si powder (blue squares) for (a) 111, (b) 422, (c) 642, and (d) 840 Bragg peaks.

Si powder. This behavior signifies microstructural contribution due to the sample effects. The diffraction patterns of both Si powders were fitted using isotropic pV profile function (as per the Supplementary Equations S1 and S2 of the supplementary file) and resulting values of FWHM and Lorentzian fraction, η, are shown in Figures 3(a) and 3(b), respectively. The observed large values of $\eta > 1$ for various experimental diffraction peaks of Si powder indicate super-Lorentzian nature of the peak profile (Wertheim et al., 1974). It is highlighted with a yellow region in Figure 3(b). Within the Voigt approximation $\eta > 1$ leads to unphysical conditions for microstructural characterization. Such observations were also made by Young and Sakthivel for simulated diffraction patterns of Si (Young and Sakthivel, 1988). These patterns were synthesized with bimodal Gaussian peak profiles having different FWHM and were analyzed using unimodal pV peak profiles. These similarities of the simulated diffraction pattern of Si powder with experimental data of present study suggest the presence of bimodal microstructure in the Si powder and signify the importance of peak shapes. Therefore, bimodal microstructural analysis was carried out. Here, the TCH profile
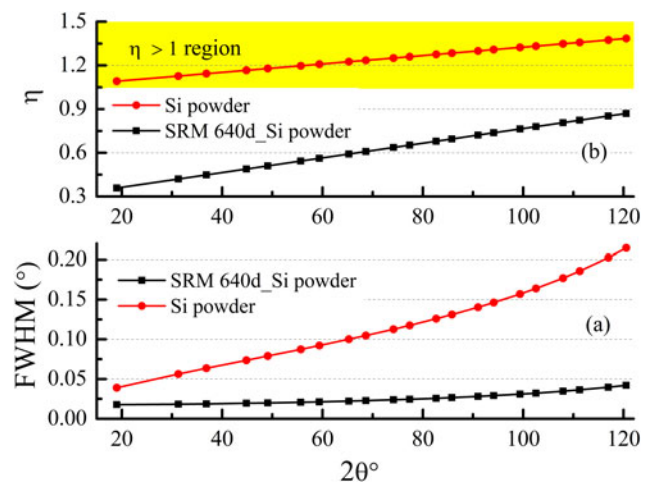

Figure 3. Comparison of angular dependency of (a) FWHM and (b) η parameters obtained from the refinement of synchrotron XRD data of SRM 640d and Si powder sample using pV profile function. pV function was chosen to model super-Lorentzian peak shapes of Si sample.

function is preferred over the pV profile for microstructural analysis because parameters [U, X and Y, I_G as per the Equations (1) and (2)] of the TCH profile function are directly related to the microstructural quantities (microstrain and crystallite size, respectively) of physical interest and limits η values between 0 and 1 (Thompson et al., 1987).

B. Microstructural characterization using TCH profile function and the Rietveld method: WPPF approach

Initially, the diffraction pattern of Si powder sample was inspected using an isotropic unimodal microstructural approach [as per Equations (1) and (2) above] of the Rietveld method. Corresponding profile fittings of a few Bragg peaks are shown in Figures 4(a), 4(c), 4(e), and 4(g) for clarity. It was observed that the peak widths and tails are overestimated while their heights are underestimated. This discrepancy increases with increasing scattering angle which indicates that the unimodal approach is not adequate. Therefore, isotropic bimodal microstructural analysis was carried out using the Rietveld method and resulting profile fittings for few Bragg peaks are shown in Figures 4(b), 4(d), 4(f), and 4(h) for comparison. The advantage of using the Rietveld method for bimodal cases is that the relative

intensities of Bragg peaks of two microstructures can be uniquely defined from the unit cell parameters, crystal symmetry, and crystal structure. This is desirable in the present study for deconvoluting the peak profile contributions of two microstructures of a bimodal approach having strongly overlapping peak positions (de Keijser et al., 1983; Delhez et al., 1988; Young and Sakthivel, 1988; Lutterotti and Scardi, 1990; Wang et al., 2015; Bhakar et al., 2016, 2017). The two microstructural components obtained from the bimodal analysis are referred to as broad and narrow profiles based on their estimated relative peak widths and are shown in Figure 5 for four Bragg peaks. Preferred orientation effect was also observed during Rietveld refinement of XRD data of SRM 640d and Si powder. Modified March's function was used as an approximation to account for preferred orientation in the [111] direction (March, 1932; Dollase, 1986) and described in detail in the supplementary file. Similar preferred orientation effect was observed by Figueiredo and Margarido in the Si phase of FeSi alloys (Figueiredo and Margarido, 1997) and also reported for the SRM 640d Si powder in the certificate of analysis (certificate Issue Date: 26 May 2010) (https://tsapps.nist.gov/srmext/certificates/archives/640d.pdf)

Same procedure was adopted for analyzing the laboratory source XRD pattern of Si powder sample and described in the supplementary file. Although the quality of unimodal fitting looks adequate (Supplementary Figure S2), still bimodal analysis was carried out to follow the findings of high-resolution synchrotron data. The parameters obtained using bimodal WPPF analyses are compared in Table I. The results of laboratory and synchrotron sources are qualitatively in agreement. It was interesting to note that the nature of size-broadening contributions of narrow and broad profiles of Si was found to be almost Gaussian-like ($\eta \sim 0$) and almost Lorentzian-like ($\eta \sim 1$), respectively, for both laboratory and synchrotron XRD data using TCH profile and double Voigt approach. In the literature, either Gaussian or Lorentzian shapes are considered for accounting the Scherrer (size) broadening effect using PBA. Also the role of mixed peak shapes (combination of Gaussian and Lorentzian, $0 < \eta < 1$) is appraised rarely in these methods (Scherrer equation, WH plot, and mWH plot)
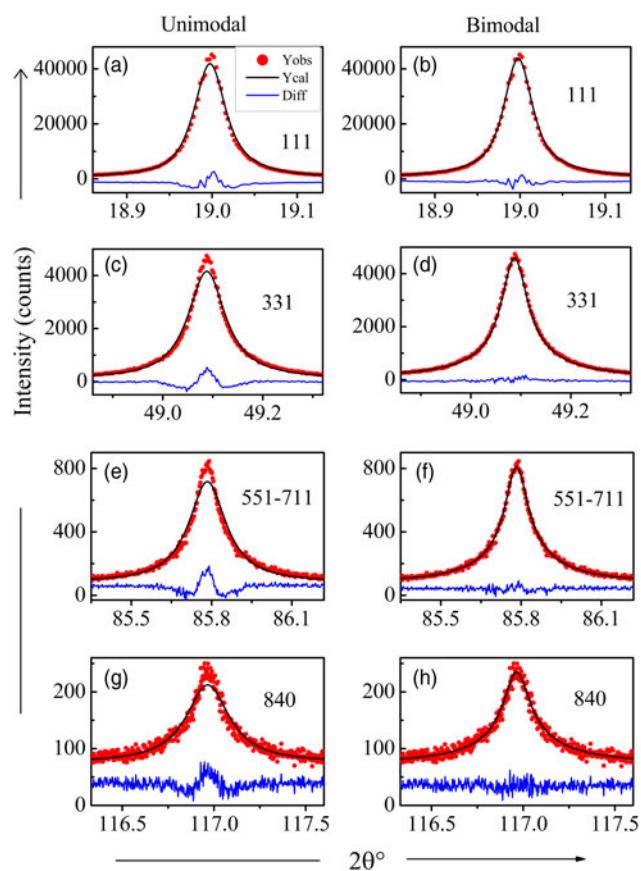

Figure 4. (a, c, e, g) Unimodal and (b, d, f, h) bimodal Rietveld refinement of 111, 331, 551–711, and 840 Bragg peaks, respectively, of synchrotron XRD data of Si powder using TCH peak profile function ($\lambda \sim 1.0353(1)$ Å). Here red circles represent the synchrotron powder XRD data, black and blue lines represent fitted curve and difference curve, respectively. Rietveld R factors (not corrected to background) are: R_p: 6.93%, R_{wp}: 8.55%, R_{exp}: 7.03%, and χ^2: 1.48 for unimodal case and R_p: 5.17%, R_{wp}: 6.77%, R_{exp}: 7.03%, and χ^2: 0.93 for bimodal case.
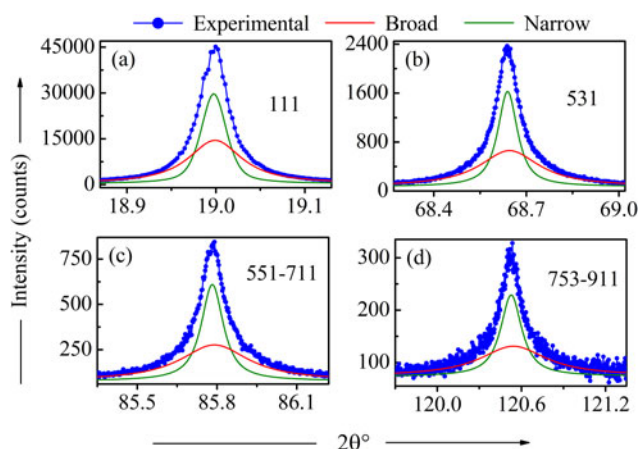

Figure 5. The observed profile (blue color) and the deconvoluted portions corresponding to the narrow (green line) and broad (red line) components of microstructures obtained using bimodal Rietveld refinement for Si powder sample ($\lambda \sim 1.0353(1)$ Å) are shown for four Bragg peaks (a) 111, (b) 531, (c) 551–711, and (d) 753–911.

TABLE I. The Rietveld refinement and WPPM parameters obtained from bimodal microstructural analysis of laboratory and synchrotron XRD data of Si powder sample are listed

Parameters	Lab XRD		Synchrotron XRD	
	Narrow profile	Broad profile	Narrow profile	Broad profile
Rietveld refinement				
Unit-cell parameter (Å)	5.4282 (3)[a]		5.4309 (2)	5.4305 (2)
ADP of Si (Å^2)[a]	0.25 (1)		0.58 (4)	
Isotropic Microstrain parameters (U, X)	0, 0.060 (2)	0, 0.26 (1)	0, 0.079 (1)	0, 0.29 (1)
Average Maximum Microstrain (10^{-4})	4.5 (1.0)	17.5 (1.0)	5.5 (1.0)	20 (1)
Isotropic size parameters (I_G, Y)	0.0049 (1), 0	0, 0.123 (4)	0.00029 (3), 0	0, 0.015 (3)
Average apparent size $L_{V\beta}$ (nm)	120 (5)	45 (10)	325 (10)	250 (50)
G_1[a]	0.86 (1)		0.89 (1)	
Weight fraction of component	0.60 (5)	0.40 (5)	0.45 (5)	0.55 (5)
Whole powder pattern modeling				
Unit-cell parameter (Å)	5.4310 (5)[a]		5.4309 (2)	5.4304 (1)
Lognormal (μ, σ)	5.1 (1), ~0.05	~0.1, 1.13 (2)	4.91 (5), 0.43 (3)	~0.1, 1.25 (3)
D_M, $s.d.$, D_S, D_V (in nm)	162 (50), 8 (3), 163(50), 163(50)	1.96 (5), 3.3(2), 27 (5), 105 (20)	150 (40), 70 (20), 220 (55), 265 (70)	2.42 (6), 4.75(3), 55(6), 270(40)
ρ (10^{15} m^{-2})	0.04 (1)	13 (1)	0.03 (1)	7.7 (1)
R_e (in nm)	110 (25)	0.95 (5)[b]	80 (10)	1.2 (1)[b]
f_E[a]	0.95(5)		0.98 (3)	
α_F, β_F (10^{-3})[a]	1.0(1), 0		0.8(1), 2.4(1)	
Weight fraction of component	0.6 (1)	0.4 (1)	0.45(5)	0.55(5)

Numbers in parentheses show the standard uncertainty of refinement. α_F and β_F are probabilities of growth and twin faults, respectively. Parameters without parenthesis are optimized and kept fixed during the final step of refinement.
[a]These parameters were constrained to be the same for both narrow and broad profiles of microstructures.
[b]This parameter value was constrained to be $D_M/2$.

(Scherrer, 1918; Williamson and Hall, 1953; Ungár and Borbély, 1996; Srikant et al., 1997). Moreover, the simultaneous presence of nearly Gaussian and Lorentzian peak profiles in a sample (e.g. Si here) using bimodal Rietveld refinement is hardly ever reported or quantified in the literature. Therefore, in order to understand this observation, a detailed microstructural analysis was carried out using an advanced WPPM approach.

C. Microstructural characterization of Si powder using the WPPM approach

For WPPM analysis, IRF was parameterized by fitting the synchrotron XRD pattern of SRM 640d Si powder using pV (analytical) expressions in PM2K software and kept fixed during microstructural analysis of Si powder. The details of the procedure adopted were the same as reported in the literature (Leoni et al., 2006; Tseng, 2017; Bhakar et al., 2021). Initially, parameters related to lognormal size distribution of spherical crystallites and dislocations were considered for modeling super-Lorentzian peak shapes of XRD pattern using a unimodal approach. The resulting WPPM fitting of few Bragg peaks is shown in Figures 6(a), 6(c), 6(e), and 6(g). It was found that at low scattering angles, the peak widths (FWHMs) are underestimated while peak heights are overestimated and this trend is reversed at high angles (i.e. the FWHMs are overestimated and peak heights are underestimated). From this observation, it is clearly evident that the peak profile and intensities of experimental XRD data of Si powder sample are not properly simulated by considering only unimodal microstructural parameters. Thus, bimodal microstructural analysis was carried out and the corresponding WPPM fitting is shown in Figures 6(b), 6(d), 6(f), and 6(h). These figures show reasonable fitting and significant improvement in the profile fitting compared to the unimodal approach. Therefore, the analysis was constrained up to a bimodal approach. Here, it is also important to mention that the profile fitting of laboratory data is improved marginally using a bimodal approach (Supplementary Figures S4 and S5), it indicates that laboratory source data are not suitable for considering multimodal cases.

During bimodal WPPM analysis, independent physical parameters for both microstructural components were modeled i.e. two lognormal size distributions and two dislocation fields were considered. In order to avoid unstable solutions, few parameters were constrained to be the same for both the microstructural components. The values of modeled parameters of physical relevance obtained using bimodal WPPM analysis are given in Table I and resulting lognormal domain size distributions are shown in Figures 7(a) and 7(b). Same procedure was adopted for WPPM analyses of the laboratory XRD data of Si powders. Its output parameters are also listed in Table I and corresponding size distributions are included in Figures 7(a) and 7(b) for comparison purposes. For the narrow profile, large $\mu \sim 5$ and small σ values were obtained while for broad profile this trend ($\mu \sim 0.1$ and $\sigma \sim 1.2$) was reversed. Therefore, it is expected that the Gaussian and Lorentzian peak profiles obtained from bimodal Rietveld refinement are related to the size distribution parameters (μ, σ) of WPPM. Using different values of size distribution parameters (μ and σ), different peak profiles are documented in the literature (Jones, 1938; Young and Sakthivel, 1988; Langford et al., 2000; Weidenthaler, 2011). But the exact relation between the different XRD peak shapes and equivalent size distribution parameters (μ and/or σ) was not explicitly conveyed. In order to probe their relationship, simulation work was carried out by Bhakar et al. considering unimodal microstructure and concluded that the nature of the diffraction peak shapes due to
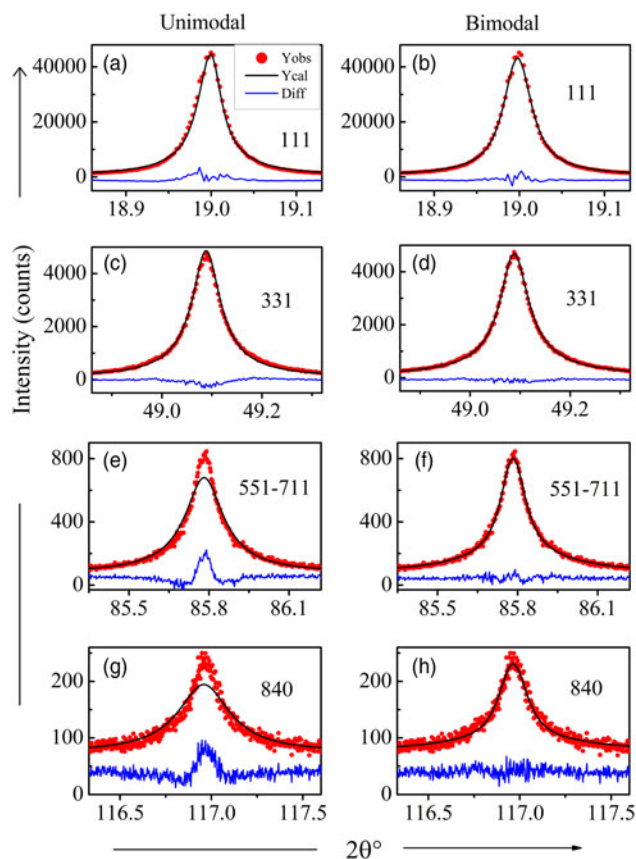
Figure 6. (a, c, e, g) Unimodal and (b, d, f, h) bimodal profile fitting of representative 111, 331, 551–711, and 840 Bragg peaks, respectively, of synchrotron XRD data of Si powder using WPPM method. Here red circles represent the synchrotron powder XRD data ($\lambda \sim 1.0353(1)$ Å), black and blue lines represent fitted curve and difference curve, respectively. R factors: WSS: 51 660, R_{wp}: 8.02%, R_{exp}: 7.03%, and χ^2: 1.3 for unimodal case and WSS: 35 000, R_{wp}: 6.6%, R_{exp}: 7.03%, and χ^2: 0.88 for bimodal case.

the size-effect is governed by the σ parameter only (Bhakar et al., 2023). Here, observed Gaussian- and Lorentzian-like natures of the size-broadening peak profiles of the Si powder are also correlating well with this lognormal variance σ of the size distribution. In this way, the XRD peak shapes (which are usually ignored in various PBA methods) derived using WPPF approach can be used as a parameter of quantitative (complementary) analysis of crystallite size distribution for such complex bimodal microstructures also. Thus, the estimation of size distribution drawn from the peak shape information obtained using the WPPF method is matching well with the WPPM results. In order to further appraise this bizarre
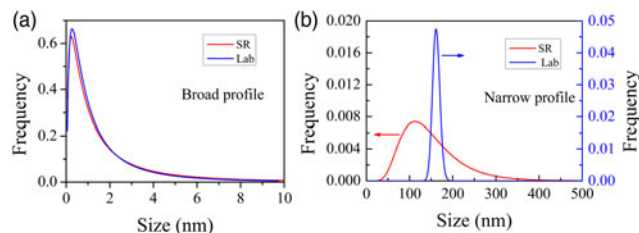

Figure 7. The lognormal size distributions of (a) broad and (b) narrow profiles of Si powder obtained using bimodal WPPM. Here red and blue lines represent distributions obtained from analysis of synchrotron (SR) and laboratory (Lab) XRD data.
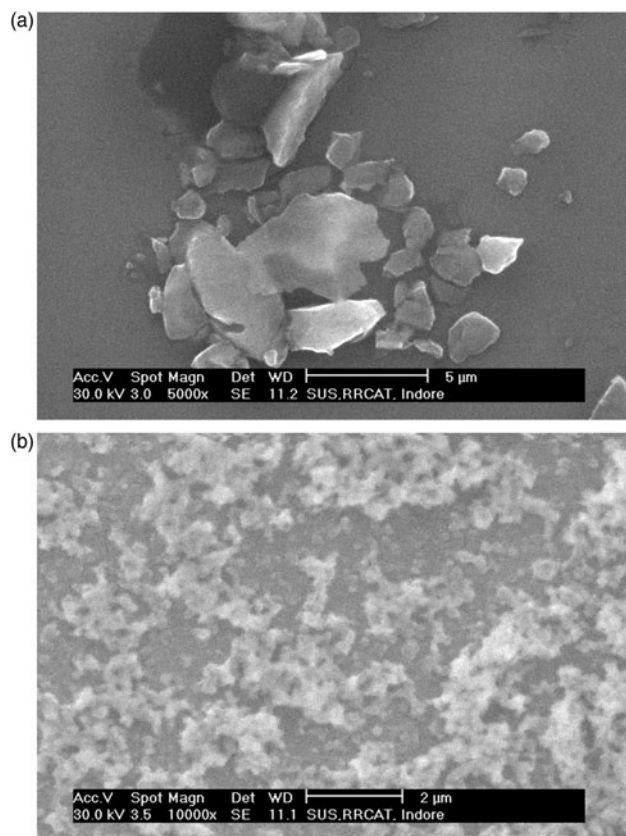

Figure 8. Two representative SEM micrographs of Si powder collected from different parts of dispersed sample signifying (a) bigger and (b) smaller particles.

microstructural behavior of this Si powder, electron microscopy methods (SEM and TEM) were used for microscopic characterization and presented in the next section.

D. Microscopy characterization of Si powder using SEM and TEM

Two representative SEM micrographs of Si powder collected from the different regions of the sample are shown in Figures 8(a) and 8(b). The first image shows the presence of bigger particles of sizes 1–7 μm, whereas in the second image, smaller particles of a few hundreds of nanometer sizes are visible. These images show that a broad distribution of particles is present in the Si powder. Figure 9(a) shows the bright field TEM image of the Si micro-particles. The selected area electron diffraction (SAED) pattern taken from one of the particles is shown in Figure 9(b). The concentric ring patterns of SAED are indexed to the polycrystalline (fcc) pattern of Si powder. Since SEM and TEM each probe a tiny amount of sample, they have limitations in the overall statistical analysis. Therefore, DLS is used for estimating particle size distribution for better statistical average and representative data is shown in Supplementary Figure S6 of the supplementary file. It gives a mean size of about 350 nm (with narrow size distribution) and in good agreement with the particle sizes of Figure 8(b) of SEM and Figure 9(a) of TEM. These observations are in contrast with XRD results. This is because WPPF and WPPM analyses of XRD data of Si powder give information about crystallite sizes while DLS, SEM, and bright-field TEM
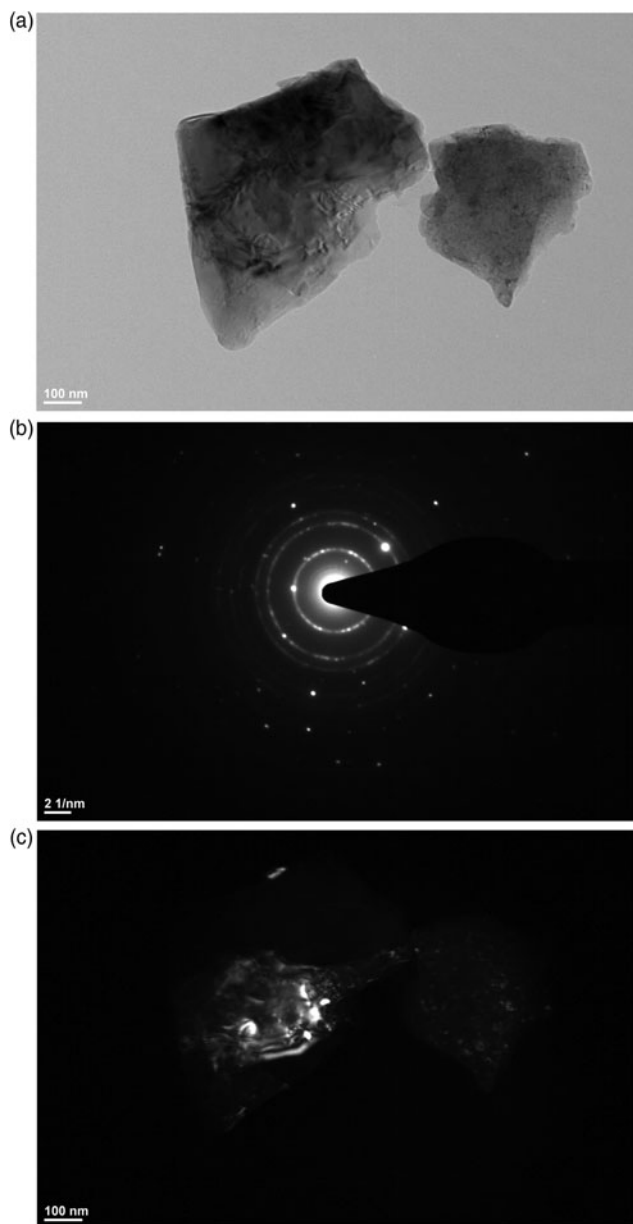
Figure 9. The representative TEM images: (a) bright field of Si powder. (b) SAED pattern showing concentric rings of diffractions spots corresponding to the polycrystalline nature of single Si particle. (c) Dark field image corresponding to (a).

correspond to the particle sizes. When the particles are made of single crystals then they coincide with the crystallite size and the results of these methods will be equivalent otherwise particle size is always greater than the crystallites. So quantitative comparison of these methods is not possible in this study for the Si powder; however, their qualitative analysis is useful to gauge the correctness of the trends obtained from the XRD analysis.

TEM is the only method of directly viewing crystallite sizes and observing a large number of SAED spots. Figure 9(b) clearly shows that the Si micro-particles are polycrystalline in nature, i.e. consists of several smaller crystallites. Therefore, in order to gauge the sizes of these crystallites, a dark-field TEM image was taken and shown in Figure 9(c). This dark field image was formed by selecting one portion of SAED and chosen randomly. An isolated bright spot in

the dark field corresponds to a single crystal. Several smaller crystallites having size of only a few nanometers can be seen in the two micro-particles. In addition, some nanoparticles of relatively bigger sizes between 50 and 100 nm range are also visible. Bigger crystallites of the order of 100's of nm size are seen in few dark-field images, which are not shown here for brevity. Since both DLS and SEM analysis give large size of particles (∼few hundred of nm) so TEM is found useful in establishing the presence of small-size crystallites as expected from the XRD analysis of the broad profile of the Si powder sample [Figure 7(a)]. TEM findings corroborate well with the XRD results that such distribution of crystallites is possible in the studied Si sample. Quantitative differences between the values of these methods (SEM, DLS, TEM, XRD) are primarily due to disparity in their measurement and analysis methodologies.

IV. DISCUSSION

XRD patterns of Si powder sample had shown super-Lorentzian peak shapes for both laboratory and synchrotron sources and their analyses using the Rietveld refinement and WPPM approach are qualitatively similar. These similarities include adequate profile fitting of the data using bimodal (narrow and broad) microstructural profiles, almost the Gaussian and the Lorentzian nature of size-broadening parts of narrow and broad peak profiles, respectively, and similar trend of their microstrain values, size distributions, and dislocation densities. It was found that the crystallite size distribution of the broad profile is almost identical for both the sources [Figure 7(a)] obtained using the WPPM method whereas for the narrow profile, it is different [Figure 7(b)]. This different behavior is mainly due to the differences in the instrumental characteristics (IRFs) of two XRD sources. Systematic comparison of the size-strain parts of bimodal microstructures is described as follows.

A. Size part of a broad profile

When the crystallite sizes are below ∼100 nm high accuracy of XRD methods is reliably achievable (Jones, 1941; Warren, 1990; Cullity and Stock, 2001; Scardi et al., 2010). Tseng had carried out WPPM studies on various nanosized Au, CuO, ZnO, and mixture of CuO/ZnO powders (D_M ranging between 2 and 5 nm, in his Ph.D thesis work) using XRD data obtained from laboratory and synchrotron sources and concluded that the size and overall defect concentration were comparable for both the sources (Tseng et al., 2015; Tseng, 2017). Also, using the results of the round-robin WPPM analysis on Fe–Mo (1.5 wt%) powder having D_M about 10 nm, Scardi et al. (2018) have shown that comparable information on the domain size distribution and microstrain can be obtained from various laboratory and synchrotron instruments despite wide variation in their IRFs (Scardi et al., 2018). These examples illustrate the observed resemblance of domain size distributions of the broad profile of the Si powder (dominated by smaller crystallites) obtained using laboratory and synchrotron sources. Similarly, Balzar et al. (2004) had performed a round-robin test on ceria samples using various X-ray and neutron diffractometers of largely different IRFs and shown that the domain size up to 25 nm was almost independent of the IRF (Balzar et al., 2004), which

again supports observations of the present work for the broad profile and assures that the results of Figure 7(a) are reliable. This similarity was due to the fact that the size-effect contribution to the peak broadening is considerably large for smaller crystallites, and feebly affected by IRF and valid for the broad profile of the Si powder. TEM findings of Figures 9(b) and 9(c) also ascertain that the Si micro-particles consist of much smaller crystallites and corroborates well with the XRD results of the broad profile. Also modeled (WPPM) large σ ($\sim$1.2) value is broadly in-line with the observed Lorentzian nature (WPPF) of this profile. It is consistent with the simulation work of Bhakar et al. on the significance of diffraction peak shapes (Bhakar et al., 2023). In this way, knowledge of XRD peak shapes is useful and provides complementary information of size distribution by using the WPPF methods.

B. Size-part of narrow profile

As crystallite size increases, the excessive peak broadening contribution arising from the size-effect starts to decrease. Therefore, the upper limit of crystallite size estimation is strongly influenced by IRF characteristics and comprehensive studies on this limit are quite limited. One of the initial assessments of the upper limit of crystallite sizes was presented by B. D. Cullity in 1956 (Cullity, 1956). It was considered as 100 nm for Debye–Scherrer cameras (XRD pattern recorded on photographic plates) and $\sim$200 nm for laboratory diffractometers. In the majority of cases, this textbook value is referred to as the upper limit of crystallite sizes. This limit is evolving with time due to the advancements in the instrumental developments (e.g. synchrotron sources) as well as improvement in the data analysis methodologies and computation programs. Recent studies show that this limit is raised to a higher range of 200–400 nm (Scardi et al., 2010). Thus, reliable estimation of the crystallite sizes is achievable in this range using the WPPM [e.g. analysis of fluorites (Broseghini et al., 2016)] and WPPF methods (e.g. analysis of four oxides of SRM 674b, https://11bm.xray.aps.anl.gov/documents/NISTSRM/NIST_SRM_676b_%5BZnO,TiO2,Cr2O3,CeO2%5D.pdf). Moreover, few dedicated studies using advanced tools in particular cases have pushed this limit further (Muniz et al., 2016; Rebuffi et al., 2017). From these studies, it could be concluded that the estimation of crystallite sizes using laboratory sources XRD data is possibly reliable up to 200 nm from WPPF and WPPM approaches (for this study, the size of the narrow profile of the Si powder, estimated at 150 nm, lies within this range). Similarly for synchrotron sources, this limit is higher and estimation of sizes up to 300 nm is expected to be quite reliable [300 nm is approximately the largest size of crystallites of the narrow profile of Si powder obtained using synchrotron data as shown in Figure 7(b)]. In addition, crystallites of bigger sizes ($\sim$100's of nm) were also observed in some dark field TEM images (not shown here) also supporting the XRD analysis of the narrow profile. It is important to emphasize that in this range deconvolution of size-broadening contribution is prone to relatively larger uncertainties compared to less than 100 nm sizes. Therefore, the accuracy of XRD methods is IRF dependent. Due to this reason, the crystallite sizes obtained from laboratory and synchrotron data are quite different for narrow profile (since peak broadening contribution was

comparable to IRF contribution) and close to the upper limit of quantification expected from corresponding IRFs.

The peak shape obtained using WPPF of the narrow profile of the Si powder (due to size-effect) was found to be almost Gaussian in nature and the corresponding σ value is expected to be close to $\sim$0.1 (Bhakar et al., 2023). This collaborates reasonably well with the σ values obtained using WPPM analysis of laboratory and synchrotron XRD data ($\sim$0 and $\sim$0.4, respectively). Thus laboratory source data suggest a narrow or mono-dispersive size distribution while better size distribution was predicted from the synchrotron XRD data. This is due to the larger q-range and higher resolution of synchrotron XRD data than laboratory data. Deb & Chatterjee had analyzed ball-milled Ni–xAl$_2$O$_3$ ($x = 0$, 0.05, 0.1) composite powders using bimodal approach and found narrow lognormal size distribution (with $\sigma \sim 0$) for one subcomponent of all samples (Deb and Chatterjee, 2019). Broseghini et al. had studied the effect of jar shapes and various milling conditions on homogenization of CaF$_2$ powder and observed bimodal distributions in many cases (Broseghini et al., 2016, 2017). One of their bimodal distributions (cylindrical shape jar-to-plate angular velocity ratio of −2 and milling time 32 h) obtained using WPPM is quite similar to the bimodal distribution of the present study. Thus existence of such vastly different crystallite size distributions of narrow and broad microstructural profiles is possible. In this way, knowledge of XRD peak shapes can be used to facilitate fair comparison of crystallite sizes obtained using different methods of WPPF and WPPM analysis. Hence, this study infers that the commonly believed non-comparability of crystallite sizes is due to negligence of peak shape contribution in WPPF methods.

C. Microstrain-part of both of the profiles

Dhara and Giri (2011) had prepared Si nanocrystals of various sizes ranging between 5 and 43 nm and analyzed them using the breadth-based mWH plot method. Their reported microstrain values lie in the range of $\sim$0.2 to 0.55% and estimated dislocation densities lie between $\sim$10^{16} and 10^{17} m^{-2}. In the present study, the observed microstrain value of the broad profile is $\sim$0.2% using WPPF and corresponding dislocation density is of the same order using WPPM i.e. $\sim$10^{16} m^{-2}. These values compare well with the literature values. For the narrow profile, a smaller microstrain value was obtained using the Rietveld refinement and corresponding smaller dislocation density was estimated from the WPPM method and given in Table I. Matej et al. had analyzed annealed equal channel angular pressing Cu sample using the bimodal approach and observed ultrafine crystallites with high dislocation density and large defect-free grains (Matěj et al., 2014). Similar trends of dislocation densities are observed in this work for both the profiles of Si powder. Such differences between the dislocation densities obtained using the mWH plot and WPPM approaches were reported for Fe powder (Bhakar et al., 2021). Thus, microstrain analysis of Si powder carried out using a bimodal approach is qualitatively in agreement for both the WPPF and WPPM methods. Quantitative differences between the two approaches are comparable to the literature and probably due to dissimilarity in their analysis methodologies (Warren, 1990; Snyder et al., 1999; Cullity and Stock, 2001; Ungár et al., 2001; Scardi et al., 2004; Gubicza, 2014) Although

this study uses well established WPPF and WPPM algorithms (which are reported to be non-comparable), still it gives the possibility of comparing them by emphasizing peak shape contribution as peak shapes are usually ignored in the WPPF approaches. Further, it is helpful in complementing PBA methods for evaluating the crystallite size distribution.

V. CONCLUSION

Detailed microstructural (size strain) characterization of XRD patterns of Si powder samples were carried out using the Rietveld refinement and WPPM approaches. Peak shapes of laboratory and synchrotron XRD patterns of Si powder were found to be super-Lorentzian in nature. This behavior was due to the presence of complex bimodal microstructures. The size-broadening contributions of narrow and broad profiles were found to be almost Gaussian and Lorentzian, respectively, from the Rietveld refinement. The size distribution parameters derived using WPPM analysis [large μ and small σ value for narrow (Gaussian-like) profile, and small μ and large σ value for broad (Lorentzian-like) profile] are responsible for this observation. In conclusion, the nature of peak shape is related to the σ parameter of size distribution and describes the physical significance of the peak shapes.

The estimated microstructural parameters, i.e., dislocation densities, D_M, R_e and phase fraction using WPPM were $\sim 0.3 \times 10^{14}\ \text{m}^{-2}$, ~ 150 nm, ~ 80 nm, and $\sim 45\%$, respectively, for the narrow profile and $\sim 8 \times 10^{14}\ \text{m}^{-2}$, ~ 2.5 nm, ~ 1 nm, and $\sim 55\%$, respectively, for the broad profile of bimodal microstructure. These are qualitatively in agreement with the Rietveld refinement results from the laboratory and synchrotron XRD data of the Si powder. For both the X-ray sources, the size distribution of the broad profile is almost identical while for the narrow profile, it is different. The volume weighted mean crystallite sizes (D_V) obtained using the laboratory and synchrotron sources are ~ 150 and ~ 325 nm, respectively, for narrow profile. This difference is due to the effect of instrumental resolutions. Combined analysis of the complementary methods of DLS, SEM, and TEM of the Si powder is found to be useful in corroborating the polydispersive nature of the Si particles and crystallite size distributions. In brief, the collective use of the width and shape of the XRD peak profile is useful in extracting detailed microstructural characteristics of the fairly complex systems.

VI. DEPOSITED DATA

Synchrotron XRD patterns of SRM 640d and as-received Si powder are deposited as (ii) "SRM_640d_SXRD.txt" and (iii) "Si_SXRD.txt", respectively. The files can be requested by contacting the Managing Editor at pdj@icdd.com.

SUPPLEMENTARY MATERIAL

The supplementary material for this article can be found at https://doi.org/10.1017/S0885715624000216.

ACKNOWLEDGEMENTS

CONFLICTS OF INTEREST

There are no conflicts to declare.

REFERENCES

Balzar, D. 1992. "Profile Fitting of X-Ray Diffraction Lines and Fourier Analysis of Broadening." *Journal of Applied Crystallography* 25 (5): 559–70. doi:10.1107/S0021889892004084.

Balzar, D. 1999. Voigt-Function Model in Diffraction Line-Broadening Analysis in R. Snyder, J. Fiala and H. J. (Eds.) *Bunge Defect and Microstructure Analysis by Diffraction* (pp. 94–126). New York, IUCr/Oxford University Press.

Balzar, D., and H. Ledbetter. 1993. "Voigt-Function Modeling in Fourier Analysis of Size- and Strain-Broadened X-Ray Diffraction Peaks." *Journal of Applied Crystallography* 26 (1): 97–103. doi:10.1107/S0021889892008987.

Balzar, D., and H. Ledbetter. 1994. "Accurate Modeling of Size and Strain Broadening in the Rietveld Refinement: The 'Double-Voigt' Approach." *Advances in X-Ray Analysis* 38 (March): 397–404. doi:10.1154/S0376030800018048.

Balzar, D., N. Audebrand, M. R. Daymond, A. Fitch, A. Hewat, J. I. Langford, A. Le Bail, D. Louër, O. Masson, C. N. McCowan, N. C. Popa, P. W. Stephens, and B. H. Toby. 2004. "Size–Strain Line-Broadening Analysis of the Ceria Round-Robin Sample." *Journal of Applied Crystallography* 37 (6): 911–24. doi:10.1107/S0021889804022551.

Baral, M., V. Srihari, A. Bhakar, M. K. Chattopadhyay, P. Tiwari, A. Chakrabarti, and T. Ganguli. 2022. "Revealing Superstructure Ordering in Co$_{1+x}$MnSb Heusler Alloys and Its Effect on Structural, Magnetic, and Electronic Properties." *Physical Review B* 105 (18): 184106. doi:10.1103/PhysRevB.105.184106.

Bhakar, A., A. H. Pandey, M. N. Singh, A. Upadhyay, A. K. Sinha, S. M. Gupta, and T. Ganguli. 2016. "Structural Analysis of Lead Magnesium Niobate Using Synchrotron Powder X-Ray Diffraction and the Rietveld Method." *Acta Crystallographica Section B: Structural Science, Crystal Engineering and Materials* 72 (June): 404–9. doi:10.1107/S2052520616006508.

Bhakar, A., A. H. Pandey, M. N. Singh, A. Upadhyay, A. K. Sinha, S. M. Gupta, T. Ganguli, and S. K. Rai. 2017. "Effect of Processing Parameters on Microstructural Properties of Lead Magnesium Niobates." *Acta Crystallographica Section B: Structural Science, Crystal Engineering and Materials* 73 (6): 1–10. doi:10.1107/S2052520617012872.

Bhakar, A., P. Gupta, P. N. Rao, M. K. Swami, P. Tiwari, T. Ganguli, and S. K. Rai. 2021. "Line Profile Analysis of Synchrotron X-Ray Diffraction Data of Iron Powder with Bimodal Microstructural Profile Parameters." *Journal of Applied Crystallography* 54 (2): 498–512. doi:10.1107/S1600576721000601.

Bhakar, A., M. Taxak, and S. K. Rai. 2023. "Significance of Diffraction Peak Shapes in Determining Crystallite Size Distribution: A Peak Shape Analysis Procedure for Pseudo-Voigt Profiles and Its Application." *Journal of Applied Crystallography* 56 (5): 1466–79. doi:10.1107/S1600576723007367.

Bhat, J. A., N. Rajora, G. Raturi, S. Sharma, P. Dhiman, S. Sanand, S. M. Shivaraj, H. Sonah, and R. Deshmukh. 2021. "Silicon Nanoparticles (SiNPs) in Sustainable Agriculture: Major Emphasis on the Practicality, Efficacy and Concerns." *Nanoscale Advances* 3 (14): 4019–28. doi:10.1039/D1NA00233C.

Bhisikar, A., M. N. Singh, N. Khantwal, and A. K. Sinha. 2022. "Effect of Microstructural Parameters of Ball-Milled Si Powder on Reactivity with Water to Produce H_2: Way Forward for on-Demand H_2 Production." *Materials Today Communications* 33 (December): 104138. doi:10.1016/J.MTCOMM.2022.104138.

Borbély, A., J. Dragomir-Cernatescu, G. Ribárik, and T. Ungár. 2003. "Computer Program ANIZC for the Calculation of Diffraction Contrast Factors of Dislocations in Elastically Anisotropic Cubic, Hexagonal and Trigonal Crystals." *Journal of Applied Crystallography* 36 (1): 160–2. http://metal.elte.hu/anizc. doi:10.1107/S0021889802021581.

Borchert, H., E. V. Shevchenko, A. Robert, I. Mekis, A. Kornowski, G. Grübel, and H. Weller. 2005. "Determination of Nanocrystal Sizes: A Comparison of TEM, SAXS, and XRD Studies of Highly Monodisperse $CoPt_3$ Particles." *Langmuir* 21 (5): 1931–36. doi:10.1021/la0477183.

Broseghini, M., M. D'Incau, L. Gelisio, N. M. Pugno, and P. Scardi. 2016. "Effect of Jar Shape on High-Energy Planetary Ball Milling Efficiency: Simulations and Experiments." *Materials and Design* 110: 365–74. doi:10.1016/j.matdes.2016.06.118.

Broseghini, M., M. D'Incau, L. Gelisio, N. M. Pugno, and P. Scardi. 2017. "Homogeneity of Ball Milled Ceramic Powders: Effect of Jar Shape and Milling Conditions." *Data in Brief* 10 (February): 186–91. doi:10.1016/j.dib.2016.11.070.

Cheng, K. Y., R. Anthony, U. R. Kortshagen, and R. J. Holmes. 2011. "High-Efficiency Silicon Nanocrystal Light-Emitting Devices." *Nano Letters* 11 (5): 1952–56. doi:10.1021/NL2001692/SUPPL_FILE/NL2001692_SI_001.PDF.

Cullity, B. D. 1956. *Elements of X-Ray Diffraction, Ch. 9.* First. USA, Addison-Wesley Publishing Company, Inc.

Cullity, B. D., and S. R. Stock. 2001. *Elements of X-Ray Diffraction, Ch. 14.* Upper Saddle River, Pearson New International.

Deb, A. K., and P. Chatterjee. 2019. "Study of Deformation Microstructure of Nickel Samples at Very Short Milling Times: Effects of Addition of α-Al_2O_3 Particles." *Journal of Theoretical and Applied Physics* 13 (1): 63–73. doi:10.1007/s40094-019-0319-2.

Deb, A. K., P. Chatterjee, and S. P. Sen Gupta. 2007. "Microstructural Characterization of Ball-Milled α-Al_2O_3: Bimodal Size Distribution and Shape Anisotropy." *Journal of Applied Crystallography* 40 (1): 33–39. doi:10.1107/S0021889806045614.

De Keijser, T. H., J. I. Langford, E. J. Mittemeijer, and A. B. Vogels. 1982. "Use of the Voigt Function in a Single-Line Method for the Analysis of X-Ray Diffraction Line Broadening." *Journal of Applied Crystallography* 15 (3): 308–14. doi:10.1107/s0021889882012035.

De Keijser, T. H., E. J. Mittemeijer, and H. C. Rozendaal. 1983. "The Determination of Crystallite-Size and Lattice-Strain Parameters in Conjunction with the Profile-Refinement Method for the Determination of Crystal Structures." *Journal of Applied Crystallography* 16 (3): 309–16. doi:10.1107/s0021889883010493.

Delhez, R., T. H. Keijser, and E. J. Mittemeijer. 1982. "Determination of Crystallite Size and Lattice Distortions through X-Ray Diffraction Line Profile Analysis-Recipes, Methods and Comments." *Fresenius' Zeitschrift Für Analytische Chemie* 312 (1): 1–16. doi:10.1007/BF00482725.

Delhez, R., T. de Keijser, E. J. Mittemeijer, and J. I. Langford. 1988. "Size and Strain Parameters for Peak Profiles: Sense and Nonsense." *Australian Journal of Physics* 41 (2): 213–27. doi:10.1071/PH880213.

Desta, D., S. K. Ram, R. Rizzoli, M. Bellettato, C. Summonte, B. R. Jeppesen, P. B. Jensen, Y. Tsao, H. Wiggers, R. N. Pereira, P. Balling, and A. N. Larsen. 2016. "Novel Back-Reflector Architecture with Nanoparticle Based Buried Light-Scattering Microstructures for Improved Solar Cell Performance." *Nanoscale* 8 (23): 12035–46. doi:10.1039/C6NR00259E.

Dhara, S., and P. K. Giri. 2011. "Size Dependent Anisotropic Strain and Optical Properties of Strained Si Nanocrystals." *Journal of Nanoscience and Nanotechnology* 11 (10): 9215–21. doi:10.1166/jnn.2011.4294.

Dollase, W. A. 1986. "Correction of Intensities for Preferred Orientation in Powder Diffractometry: Application of the March Model." *Journal of Applied Crystallography* 19 (4): 267–72. doi:10.1107/S0021889886089458.

Dutta, M., L. Thirugnanam, P. V. Trinh, and N. Fukata. 2015. "High Efficiency Hybrid Solar Cells Using Nanocrystalline Si Quantum Dots and Si Nanowires." *ACS Nano* 9 (7): 6891–99. doi:10.1021/ACSNANO.5B03268/SUPPL_FILE/NN5B03268_SI_001.PDF.

Ectors, D., and J. Neubauer. 2015. "Domain Size Anisotropy in the Double-Voigt Approach: An Extended Model Short Communications." *Journal of Applied Crystallography* 48: 1998–2001. doi:10.1107/S1600576715018488.

Ectors, D., F. Goetz-Neunhoeffer, and J. Neubauer. 2017. "Routine (an) Isotropic Crystallite Size Analysis in the Double-Voigt Approximation Done Right?" *Powder Diffraction* 32 (S1): S27–34. doi:10.1017/S0885715617000070.

Erogbogbo, F., K. T. Yong, I. Roy, R. Hu, W. C. Law, W. Zhao, H. Ding, F. Wu, R. Kumar, M. T. Swihart, and P. N. Prasad. 2011. "In Vivo Targeted Cancer Imaging, Sentinel Lymph Node Mapping and Multi-Channel Imaging with Biocompatible Silicon Nanocrystals." *ACS Nano* 5 (1): 413–23. doi:10.1021/NN1018945/SUPPL_FILE/NN1018945_SI_001.PDF.

Erogbogbo, F., T. Lin, P. M. Tucciarone, K. M. Lajoie, L. Lai, G. D. Patki, P. N. Prasad, and M. T. Swihart. 2013. "On-Demand Hydrogen Generation Using Nanosilicon: Splitting Water without Light, Heat, or Electricity." *Nano Letters* 13 (2): 451–56. doi:10.1021/NL304680W/SUPPL_FILE/NL304680W_SI_001.PDF.

Figueiredo, M. O., and F. Margarido. 1997. "Silicon in Fe-Si Alloys: Correction of X-Ray Intensities for Preferred Orientation." *Textures and Microstructures* 29 (1–2): 77–87. doi:10.1155/TSM.29.77.

Finger, L. W., D. E. Cox, and A. P. Jephcoat. 1994. "A Correction for Powder Diffraction Peak Asymmetry Due to Axial Divergence." *Journal of Applied Crystallography* 27 (6): 892–900. doi:10.1107/S0021889894004218.

Garnier, E., F. J. Vidal-Iglesias, J. M. Feliu, and J. Solla-Gullón. 2019. "Surface Structure Characterization of Shape and Size Controlled Pd Nanoparticles by Cu UPD: A Quantitative Approach." *Frontiers in Chemistry* 7 (July): 1–11. doi:10.3389/fchem.2019.00527.

Gubicza, J. 2014. *X-Ray Line Profile Analysis in Materials Science.* Hershey, PA, IGI Global. doi:10.4018/978-1-4666-5852-3.

Gubicza, J., J. Szépvölgyi, I. Mohai, L. Zsoldos, and T. Ungár. 2000. "Particle Size Distribution and Dislocation Density Determined by High Resolution X-Ray Diffraction in Nanocrystalline Silicon Nitride Powders." *Materials Science and Engineering: A* 280 (2): 263–69. doi:10.1016/S0921-5093(99)00702-9.

Gupta, P., P. N. Rao, M. K. Swami, A. Bhakar, S. Lal, S. R. Garg, C. K. Garg, P. K. Gauttam, S. R. Kane, V. K. Raghuwanshi, and S. K. Rai. 2021. "BL-02: A Versatile X-Ray Scattering and Diffraction Beamline for Engineering Applications at Indus-2 Synchrotron Source." *Journal of Synchrotron Radiation* 28 (4): 1193–201. doi:10.1107/S1600577521004690.

Ida, T., S. Shimazaki, H. Hibino, and H. Toraya. 2003. "Diffraction Peak Profiles from Spherical Crystallites with Lognormal Size Distribution." *Journal of Applied Crystallography* 36 (5): 1107–15. doi:10.1107/S0021889803011580.

Iyer, S. S., and Y. H. Xie. 1993. "Light Emission from Silicon." *Science* 260 (5104): 40–46. doi:10.1126/science.260.5104.40.

Jones, F. W. 1938. "The Measurement of Particle Size by the X-Ray Method." *Proceedings of the Royal Society of London. Series A. Mathematical and Physical Sciences* 166 (924): 16–43. doi:10.1098/RSPA.1938.0079.

Jones, F. W. 1941. "Particle Size Measurement by the X-Ray Method." *Journal of Scientific Instruments* 18 (7): 157. doi:10.1088/0950-7671/18/7/314.

Kaduk, J. A., S. J. L. Billinge, R. E. Dinnebier, N. Henderson, I. Madsen, R. Černý, M. Leoni, L. Lutterotti, S. Thakral, and D. Chateigner. 2021. "Powder Diffraction." *Nature Reviews Methods Primers* 1 (1): 77. doi:10.1038/s43586-021-00074-7.

Klug, H. P., & L. E. Alexander. 1974. *X-Ray Diffraction Procedures: for Polycrystalline and Amorphous Materials.* 2nd ed. John Willey, John Wiley & Sons. https://ui.adsabs.harvard.edu/abs/1974xdpf.book.....K/abstract.

Langford, J. I. 1978. "A Rapid Method for Analysing the Breadths of Diffraction and Spectral Lines Using the Voigt Function." *Journal of Applied Crystallography* 11 (1): 10–14. doi:10.1107/S0021889878012601/FULL.

Langford, J. I., R. Delhez, T. H. De Keijser, and E. J. Mittemeijer. 1988. "Profile Analysis for Microcrystalline Properties by the Fourier and Other Methods." *Australian Journal of Physics* 41 (2): 173. doi:10.1071/PH880173.

Langford, J. I., D. Louër, and P. Scardi. 2000. "Effect of a Crystallite Size Distribution on X-Ray Diffraction Line Profiles and Whole-Powder-Pattern Fitting." *Journal of Applied Crystallography* 33 (3 II): 964–74. doi:10.1107/S002188980000460X.

Le Bail, A., H. Duroy, and J. L. Fourquet. 1988. "Ab-Initio Structure Determination of $LiSbWO_6$ by X-Ray Powder Diffraction." *Materials Research Bulletin* 23 (3): 447–52. doi:10.1016/0025-5408(88)90019-0.

Leoni, M., T. Confente, and P. Scardi. 2006. PM2K: A Flexible Program Implementing Whole Powder Pattern Modelling. in Ninth European Powder Diffraction Conference (Vol. 1, pp. 249–54). Oldenbourg Wissenschaftsverlag. doi:10.1524/9783486992526-043.

Lutterotti, L., and P. Scardi. 1990. "Simultaneous Structure and Size-Strain Refinement by the Rietveld Method." *Journal of Applied Crystallography* 23 (4): 246–52. doi:10.1107/S0021889890002382.

March, A. 1932. "Mathematische Theorie Der Regelung Nach Der Korngestah Bei Affiner Deformation." *Zeitschrift Für Kristallographie - Crystalline Materials* 81 (1–6): 285–97. doi:10.1524/zkri.1932.81.1.285.

Matěj, Z., A. Kadlecová, M. Janeček, L. Matějová, M. Dopita, and R. Kužel. 2014. "Refining Bimodal Microstructure of Materials with MSTRUCT." *Powder Diffraction* 29 (S2): S35–41. doi:10.1017/S0885715614000852.

Matyi, R. J., L. H. Schwartz, and J. B. Butt. 1987. "Particle Size, Particle Size Distribution, and Related Measurements of Supported Metal Catalysts." *Catalysis Reviews* 29 (1): 41–99. doi:10.1080/01614948708067547.

Miller, D. A. B. 1995. "Silicon Sees the Light." *Nature* 378 (6554): 238. doi:10.1038/378238a0.

Mittemeijer, E. J., and P. Scardi. 2004. *Diffraction Analysis of the Microstructure of Materials*. E. J. Mittemeijer, and P. Scardi (Eds.) Springer Series in Materials Science. (Vol. 68). Berlin, Heidelberg: Springer Berlin Heidelberg. doi:10.1007/978-3-662-06723-9.

Mourdikoudis, S., R. M. Pallares, and N. T. K. Thanh. 2018. "Characterization Techniques for Nanoparticles: Comparison and Complementarity upon Studying Nanoparticle Properties." *Nanoscale* 10 (27): 12871–934. doi:10.1039/C8NR02278J.

Muniz, F. T., M. R. Miranda, C. Morilla dos Santos, and J. M. Sasaki. 2016. "The Scherrer Equation and the Dynamical Theory of X-Ray Diffraction Research Papers." *Acta Crystallographica Section A Foundations and Advances* 72 (1): 385–90. doi:10.1107/S205327331600365X.

Nandi, R. K., and S. P. Sen Gupta. 1978. "The Analysis of X-Ray Diffraction Profiles from Imperfect Solids by an Application of Convolution Relations." *Journal of Applied Crystallography* 11 (1): 6–9. doi:10.1107/S0021889878012595.

National Institute of Standards & Technology (NIST). 2010. Standard Reference Material® 640d. no. May: 1–5. https://Tsapps.Nist.Gov/Srmext/Certificates/Archives/640d.Pdf.

Pavesi, L., L. Dal Negro, C. Mazzoleni, G. Franzò, and F. Priolo. 2000. "Optical Gain in Silicon Nanocrystals." *Nature* 408 (6811): 440–44. doi:10.1038/35044012.

Peng, F., Y. Su, Y. Zhong, C. Fan, S. T. Lee, and Y. He. 2014. "Silicon Nanomaterials Platform for Bioimaging, Biosensing, and Cancer Therapy." *Accounts of Chemical Research* 47 (2): 612–23. doi:10.1021/AR400221G/ASSET/IMAGES/MEDIUM/AR-2013-00221G_0011.GIF.

Popa, N. C., and D. Balzar. 2002. "An Analytical Approximation for a Size-Broadened Profile given by the Lognormal and Gamma Distributions." *Journal of Applied Crystallography* 35 (3): 338–46. doi:10.1107/S0021889802004156.

Popa, N. C., and D. Balzar. 2008. "Size-Broadening Anisotropy in Whole Powder Pattern Fitting. Application to Zinc Oxide and Interpretation of the Apparent Crystallites in Terms of Physical Models." *Journal of Applied Crystallography* 41 (3): 615–27. doi:10.1107/S0021889808012223.

Ram, S. K., M. N. Islam, S. Kumar, and P. Roca i Cabarrocas. 2009. "Evidence of Bimodal Crystallite Size Distribution in Mc-Si:H Films." *Materials Science and Engineering: B* 159–160 (C): 34–37. doi:10.1016/J.MSEB.2008.11.048.

Rastogi, A., D. K. Tripathi, S. Yadav, D. K. Chauhan, M. Živčák, M. Ghorbanpour, N. I. El-Sheery, and M. Brestic. 2019. "Application of Silicon Nanoparticles in Agriculture." *3 biotech* 9 (3): 90. doi:10.1007/s13205-019-1626-7.

Rebuffi, L., M. Sa, E. Busetto, and P. Scardi. 2017. "Understanding the Instrumental Profile of Synchrotron Radiation X-Ray Powder Diffraction Beamlines Research Papers." *Journal of Synchrotron Radiation* 24: 622–35. doi:10.1107/S1600577517005434.

Ribárik, G., B. Jóni, and T. Ungár. 2020. "The Convolutional Multiple Whole Profile (CMWP) Fitting Method, a Global Optimization Procedure for Microstructure Determination." *Crystals* 10 (7): 623. doi:10.3390/cryst10070623.

Rietveld, H. M. 1967. "Line Profiles of Neutron Powder-Diffraction Peaks for Structure Refinement." *Acta Crystallographica* 22 (1): 151–52. doi:10.1107/S0365110X67000234.

Rietveld, H. M. 1969. "A Profile Refinement Method for Nuclear and Magnetic Structures." *Journal of Applied Crystallography* 2 (2): 65–71. doi:10.1107/S0021889869006558.

Rodríguez-Carvajal, J. 1993. "Recent Advances in Magnetic Structure Determination by Neutron Powder Diffraction." *Physica B: Condensed Matter* 192 (1–2): 55–69. doi:10.1016/0921-4526(93)90108-I.

Rodríguez-Carvajal, J., and T. Roisnel. 2004. "Line Broadening Analysis Using FullProf*: Determination of Microstructural Properties." *Materials Science Forum* 443–444 (January): 123–26. doi:10.4028/www.scientific.net/MSF.443-444.123.

Sánchez-Bajo, F., A. L. Ortiz, and F. L. Cumbrera. 2006. "Analytical Formulation of the Variance Method of Line-Broadening Analysis for Voigtian X-Ray Diffraction Peaks." *Journal of Applied Crystallography* 39 (4): 598–600. doi:10.1107/S0021889806017122.

Scardi, P. 2002. "Profile Modelling versus Profile Fitting in Powder Diffraction." *Zeitschrift Für Kristallographie - Crystalline Materials* 217 (7–8): 420–21. doi:10.1524/zkri.217.7.420.23656.

Scardi, P. 2020. "Diffraction Line Profiles in the Rietveld Method." *Crystal Growth & Design* 20 (10): 6903–16. doi:10.1021/acs.cgd.0c00956.

Scardi, P., and M. Leoni. 2002. "Whole Powder Pattern Modelling." *Acta Crystallographica Section A Foundations of Crystallography* 58 (2): 190–200. doi:10.1107/S0108767301021298.

Scardi, P., M. Leoni, and Y. H. Dong. 2000. "Whole Diffraction Pattern-Fitting of Polycrystalline Fcc Materials Based on Microstructure." *European Physical Journal B* 18 (1): 23–30. doi:10.1007/s100510070073.

Scardi, P., Y. H. Dong, and M. Leoni. 2001. "Line Profile Analysis in the Rietveld Method and Whole-Powder-Pattern Fitting." *Materials Science Forum* 378–381 (I): 132–41. doi:10.4028/www.scientific.net/msf.378-381.132.

Scardi, P., M. Leoni, and R. Delhez. 2004. "Line Broadening Analysis Using Integral Breadth Methods: A Critical Review." *Journal of Applied Crystallography* 37 (3): 381–90. doi:10.1107/S0021889804004583.

Scardi, P., M. Leoni, and J. Faber. 2006. "Diffraction Line Profile from a Disperse System: A Simple Alternative to Voigtian Profiles." *Powder Diffraction* 21 (4): 270–77. doi:10.1154/1.2358359.

Scardi, P., M. Ortolani, and M. Leoni. 2010. "WPPM: Microstructural Analysis beyond the Rietveld Method." *Materials Science Forum* 651 (May): 155–71. doi:10.4028/www.scientific.net/MSF.651.155.

Scardi, P., M. Ermrich, A. Fitch, E.-W. Huang, R. Jardin, R. Kuzel, A. Leineweber, A. Mendoza Cuevas, S. T. Misture, L. Rebuffi, and C. Schimpf. 2018. "Size–Strain Separation in Diffraction Line Profile Analysis." *Journal of Applied Crystallography* 51 (3): 831–43. doi:10.1107/S1600576718005411.

Scherrer, P. 1918. "Bestimmung Der Größe Und Der Inneren Struktur von Kolloidteilchen Mittels Röntgenstrahlen." *Nachr Ges Wiss Goettingen, Math. Phys* 2: 98–100. https://cir.nii.ac.jp/crid/1573105975714168704.

Snyder, R. L., J. Fiala, and H. J. Bunge, (eds.) 1999. *Defect and Microstructure Analysis by Diffraction* (Vol. 200). International Union of Crystallography. New York, Oxford University Press.

Srikant, V., J. S. Speck, and D. R. Clarke. 1997. "Mosaic Structure in Epitaxial Thin Films Having Large Lattice Mismatch." *Journal of Applied Physics* 82 (9): 4286–95. doi:10.1063/1.366235.

Su, X., Q. Wu, J. Li, X. Xiao, A. Lott, W. Lu, B. W. Sheldon, and J. Wu. 2014. "Silicon-Based Nanomaterials for Lithium-Ion Batteries: A Review." *Advanced Energy Materials* 4 (1): 1300882. doi:10.1002/AENM.201300882.

Thakral, S., M. W. Terban, N. K. Thakral, and R. Suryanarayanan. 2016. "Recent Advances in the Characterization of Amorphous Pharmaceuticals by X-Ray Diffractometry." *Advanced Drug Delivery Reviews* 100 (May): 183–93. doi:10.1016/j.addr.2015.12.013.

Thompson, P., D. E. Cox, and J. B. Hastings. 1987. "Rietveld Refinement of Debye–Scherrer Synchrotron X-Ray Data from Al_2O_3." *Journal of Applied Crystallography* 20 (2): 79–83. doi:10.1107/S0021889887087090.

Tseng, J. C. 2017. Microstructure Analysis of Nanosized Materials Based on X-Ray Diffraction Study: A Practical Protocol. Ruhr-Univertität Bochum.

Tseng, J. C., W. Schmidt, U. Sager, E. Däuber, A. Pommerin, and C. Weidenthaler. 2015. "Microstructure Analysis of Complex CuO/ZnO@carbon Adsorbers: What Are the Limits of Powder Diffraction Methods?" *Physical Chemistry Chemical Physics* 17 (18): 12282–91. doi:10.1039/c5cp01135c.

Ungár, T., and A. Borbély. 1996. "The Effect of Dislocation Contrast on X-Ray Line Broadening: A New Approach to Line Profile Analysis." *Applied Physics Letters* 69 (21): 3173–75. doi:10.1063/1.117951.

Ungár, T., M. Leoni, and P. Scardi. 1999. "The Dislocation Model of Strain Anisotropy in Whole Powder-Pattern Fitting: The Case of an Li-Mn Cubic Spinel." *Journal of Applied Crystallography* 32 (2): 290–95. doi:10.1107/S0021889898012710.

Ungár, T., J. Gubicza, G. Ribárik, and A. Borbély. 2001. "Crystallite Size Distribution and Dislocation Structure Determined by Diffraction Profile Analysis: Principles and Practical Application to Cubic and Hexagonal Crystals." *Journal of Applied Crystallography* 34 (3): 298–310. doi:10.1107/S0021889801003715.

Uvarov, V., and I. Popov. 2015. "An Estimation of the Correctness of XRD Results Obtained from the Analysis of Materials with Bimodal Crystallite Size Distribution." *Crystengcomm* 17 (43): 8300–6. doi:10.1039/C5CE01799H.

Wang, X., J. Li, R. G. McDonald, A. Van Riessen, and R. D. Hart. 2015. "X-Ray Diffraction Line Profile Analysis of Acid-Resistant Goethite in Western Australian Nickel Laterite Ore." *Journal of Applied Crystallography* 48: 814–26. doi:10.1107/S1600576715006275.

Warren, B. E. 1990. *X-Ray Diffraction*. New York, Dover Publications, INC.

Warren, B. E., and B. L. Averbach. 1950. "The Effect of Cold-Work Distortion on X-Ray Patterns." *Journal of Applied Physics* 21 (6): 595–99. doi:10.1063/1.1699713.

Weidenthaler, C. 2011. "Pitfalls in the Characterization of Nanoporous and Nanosized Materials." *Nanoscale* 3 (3): 792–810. doi:10.1039/c0nr00561d.

Wertheim, G. K., M. A. Butler, K. W. West, and D. N. E. Buchanan. 1974. "Determination of the Gaussian and Lorentzian Content of Experimental Line Shapes." *Review of Scientific Instruments* 45 (11): 1369–71. doi:10.1063/1.1686503.

Wilkens, M. 1970. "The Determination of Density and Distribution of Dislocations in Deformed Single Crystals from Broadened X-ray Diffraction Profiles." *Physica Status Solidi (A)* 2 (2): 359–70. doi:10.1002/pssa.19700020224.

Wilkens, M. 1987. "X-ray Line Broadening and Mean Square Strains of Straight Dislocations in Elastically Anisotropic Crystals of Cubic Symmetry." *Physica Status Solidi (A)* 104 (1): K1–6. doi:10.1002/pssa.2211040137.

Williamson, G. K., and W. H. Hall. 1953. "X-Ray Line Broadening from Filed Aluminium and Wolfram." *Acta Metallurgica* 1 (1): 22–31. doi:10.1016/0001-6160(53)90006-6.

Young, R. A., and A. Sakthivel. 1988. "Bimodal Distributions of Profile-Broadening Effects in Rietveld Refinement." *Journal of Applied Crystallography* 21 (5): 416–25. doi:10.1107/S0021889888004091.

Zhang, C., F. Wang, J. Han, S. Bai, J. Tan, J. Liu, and F. Li. 2021. "Challenges and Recent Progress on Silicon-Based Anode Materials for Next-Generation Lithium-Ion Batteries." *Small Structures* 2 (6): 2100009. doi:10.1002/SSTR.202100009.